Enhanced slip on a patterned substrate due to depinning of contact line

Peng Gao[1] and James J. Feng[1,2,a)]
[1]*Department of Chemical and Biological Engineering, University of British Columbia, Vancouver, British Columbia V6T 1Z3, Canada*
[2]*Department of Mathematics, University of British Columbia, Vancouver, British Columbia V6T 1Z2, Canada*

(Received 14 June 2009; accepted 6 October 2009; published online 26 October 2009)

We perform numerical simulations of a shear flow over a periodically patterned substrate with entrapped gas bubbles. A diffuse-interface model is employed to handle the liquid-gas interface deformation and the three-phase contact line. Depending on the shear rate and the pattern geometry, four flow regimes are observed. The contact lines can be pinned, depinned, or eliminated depending on the competition between the shear force and the surface tension. The effective slip length is found to be dependent on the morphology of the menisci and hence on the shear rate. In particular, the bubbles are transformed into a continuous gas film when the shear rate is larger than a critical value, resulting in a significantly enhanced slip length proportional to the liquid-gas viscosity ratio. The present results have interesting implications for effective slip on superhydrophobic surfaces.
 [doi:10.1063/1.3254253]

I. INTRODUCTION

Recent development of micro- and nanofluidic devices has prompted a re-examination of the fluid-solid boundary condition, and there is mounting evidence from experiments as well as numerical simulations for slippage on solid walls.[1,2] From a practical viewpoint, wall slip may be desirable because of reduction in flow resistance or undesirable because of suppressed dispersion or mixing.

The amount of wall slip is commonly represented by the slip length b, defined using Navier's law,

$$v_s = b\dot{\gamma}_w, \tag{1}$$

where v_s is the slip velocity and $\dot{\gamma}_w$ is the shear rate at the wall. Typically, b is on the order of a few tens of nanometers on smooth surfaces,[3–5] and is too small to produce a significant modification of the microscale flow. Experimenters have achieved much greater slip on two types of modified substrates: smooth hydrophobic surfaces[6,7] and microtextured surfaces with topological patterns such as posts, grooves, and cavities.[8] In the former case, it is believed that nanobubbles are entrapped on the surface because of the poor wettability and they play a central role in generating large slip.[9–11] In the latter case, the surface texture is designed expressly to produce micron-sized bubbles or a gas layer, and such "superhydrophobic" surfaces are often likened to the lotus leaf. In both cases, the low-viscosity gas bubbles act as a lubricant so that the liquid can slide on them, resulting in large slippage. Of course, such slippage should be regarded as "apparent" or "effective" slip due to the interface with a low-viscosity gas, and differs from the true slip between the liquid and solid molecules.[12] With optimal designs, micropatterned substrates have exhibited slip length of tens and even hundreds of microns,[13,14] and a number of experimental,[15–17] computational,[18–20] and theoretical[21,22] studies have been devoted to superhydrophobicity and the associated large slippage.

A somewhat controversial aspect of such bubble-induced slip is how b depends on the imposed shear rate $\dot{\gamma}$. Most experiments performed in microchannels showed an essentially constant b, unaffected by $\dot{\gamma}$.[13,16,23,24] However, Choi *et al.*[4] observed a linear increase in b with $\dot{\gamma}$ on smooth hydrophobic surfaces. What seems to distinguish this study from the others is that they have used particularly small channel heights (~ 1 μm) and therefore achieved higher shear rates $\dot{\gamma} \sim 10^5/\mathrm{s}$. In addition, experiments performed with the atomic force microscope (AFM) and the surface force apparatus (SFA) have also reported strong increase in b with $\dot{\gamma}$ at high shear rate.[3,6] In both the AFM and SFA setup, two solid walls are squeezed toward each other to induce drainage flow in the narrow gap at shear rates as high as $\dot{\gamma} \sim 10^4/\mathrm{s}$. However, it is unclear at present whether the apparent slip in the AFM and SFA experiments is of the same origin as in shear flows in microchannels. In fact, Lauga and Brenner[25] and Steinberger *et al.*[26] demonstrated that the increasing hydrostatic pressure during squeezing flows, coupled with the compressibility of the gas phase, can account for the apparent dependence of b on $\dot{\gamma}$.

Since the slippage is induced by the gas bubbles, it is reasonable to expect b to depend on the morphology of the gas-liquid interface. There seems to be no experimental observation or data in the literature on how the interfacial morphology affects the apparent slip. Besides the small spatial dimensions, the scarcity of experimental results may be because of the very high shear rates required to deform small substrate-bound bubbles.[21] To our knowledge, the only investigation so far is the lattice-Boltzmann simulation of Hyväluoma and Harting[27] of a shear flow over an entrapped bubble. With the contact line pinned on the solid substrate, their results show that the bubble deformation due to external shear causes the slip length b to *decrease* significantly with $\dot{\gamma}$. This contradicts experimental data showing b increasing

a)Author to whom correspondence should be addressed. Electronic mail: jfeng@chbe.ubc.ca.

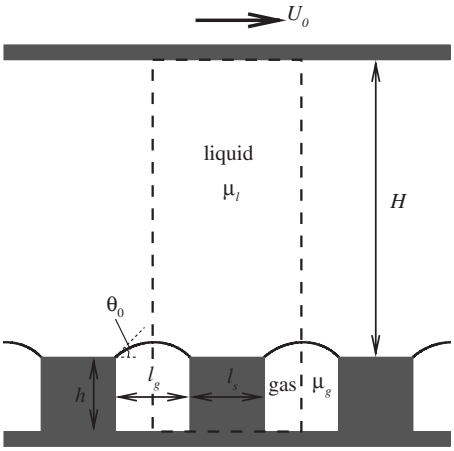

FIG. 1. Schematic of the flow geometry. The dashed lines mark the computational domain, which is periodic in the horizontal direction.

with $\dot{\gamma}$.[4,28] Therefore, the question of how bubble-induced apparent slip depends on the shear rate appears to be unresolved.

Here we propose a mechanism based on shear-induced depinning of the contact line which may explain the shear enhancement of slip over bubbles. This is based on the following physical picture. A bubble pinned onto the edges of surface roughness will be deformed at high flow rates. If the substrate is hydrophobic, the contact lines may be depinned relatively easily to allow the bubble to spread or even slide along the substrate, thereby augmenting the apparent slip. This scenario is explored by performing two-dimensional (2D) simulations of a shear flow over a periodic topology, with low-viscosity bubbles being trapped in equally spaced rectangular grooves.

II. PROBLEM SETUP AND NUMERICAL METHOD

Consider a Newtonian liquid confined in a microchannel of height H with a smooth upper wall and a roughly patterned lower wall, as illustrated in Fig. 1. In two dimensions, the roughness is represented by spatially periodic ridges or grooves. The width and depth of the groove are l_g and h, respectively, and the ridge width is l_s. We assume the liquid-solid contact to be in the Cassie state with gas bubbles trapped in the grooves. The volume of the entrapped gas is prescribed by the equilibrium "protrusion angle" θ_0. Under flow, the protrusion angle will deviate from θ_0 and differ between the contact lines upstream and downstream of the groove. The gas is treated as an incompressible fluid with a viscosity μ_g that is much smaller than the liquid viscosity μ_l. Inertia is negligible and the liquid-gas density ratio plays no role. The flow is driven by the upper wall moving in its own plane with a constant velocity U_0 and the lower wall being stationary.

This setup ensures the presence of entrapped bubbles that protrude into the liquid. As will be seen shortly, the protruding menisci play key roles in the phenomena of interest here. As such, we should point out several assumptions implied by this setup. First, real surface textures may consist of pillars or cavities. Our geometry assumes the 2D counterpart of the latter. Thus, the bubbles are bounded and isolated, in contrast to the interconnected gas network formed by pillars.[8] Second, we have neglected loss of the gas into the liquid by diffusion or vapor condensation. In reality, such mechanisms tend to deplete the gas pocket and diminish the effects to be discussed.[29] Finally, we have assumed a sufficient amount of trapped gas such that the meniscus protrudes into the liquid. If the meniscus is flat or even concave ($\theta_0 \leq 0$), no contact line depinning occurs and the gas cannot greatly enhance apparent slippage. In reality, the amount of gas trapped in cavities depends on how the liquid is applied over the substrate, and has a critical effect on superhydrophobicity and slippage.[29]

The computational domain is the unit cell enclosed by the dashed line in Fig. 1, and periodic boundary conditions are employed at the inlet and the outlet. To obtain the apparent slip length b, we calculate the average shear rate at the upper wall, $\dot{\gamma}_w$, and then determine the slip length by

$$b = \left(\frac{\dot{\gamma}_0}{\dot{\gamma}_w} - 1 \right) H, \tag{2}$$

where $\dot{\gamma}_0 = U_0/H$ is the nominal shear rate of a Couette flow.[27]

The liquid-gas interface and the moving contact line are modeled by a diffuse-interface method.[30,31] We introduce an order parameter ϕ such that $\phi=1$ in the liquid and $\phi=-1$ in the gas. The position of the interface is given by $\phi=0$ and ϕ varies smoothly across the interface. The convection and diffusion of ϕ are governed by the Cahn–Hilliard equation

$$\frac{\partial \phi}{\partial t} + \boldsymbol{v} \cdot \nabla \phi = \nabla \cdot (M \nabla G), \tag{3}$$

where M is the mobility, $\boldsymbol{v}$ is the velocity vector, and $G = \lambda[-\nabla^2 \phi + (\phi^2 - 1)\phi/\epsilon^2]$ is the bulk chemical potential. λ is the mixing energy density and ϵ is a measure of the interface thickness; in equilibrium they are related to the surface tension σ by

$$\sigma = \frac{2\sqrt{2}}{3} \frac{\lambda}{\epsilon}. \tag{4}$$

In the absence of inertia, the flow is governed by the continuity equation and a modified Stokes equation,

$$\nabla \cdot \boldsymbol{v} = 0, \tag{5}$$

$$-\nabla p + \nabla \cdot (\mu \nabla \boldsymbol{v}) + G \nabla \phi = 0, \tag{6}$$

where p is the pressure, $\mu = \frac{1}{2}(1+\phi)\mu_l + \frac{1}{2}(1-\phi)\mu_g$, and the $G\nabla\phi$ term represents the contribution of the surface tension.

The wettability of the substrate is described by a wall energy f_w that discriminates between the two fluid components,[30]

$$f_w(\phi) = -\sigma \cos\theta_S \frac{\phi(3-\phi^2)}{4} + \frac{\sigma_{ls} + \sigma_{gs}}{2}, \tag{7}$$

where θ_S is the static contact angle determined by Young's equation $\sigma_{gs} - \sigma_{ls} = \sigma \cos\theta_S$, σ_{ls} and σ_{gs} being the liquid- and gas-solid interfacial tensions, respectively. Then the following boundary conditions may be imposed on the solid substrate:[32]

$$\boldsymbol{v} = \boldsymbol{v}_w, \tag{8}$$

$$\boldsymbol{n} \cdot \nabla G = 0, \tag{9}$$

$$\lambda \boldsymbol{n} \cdot \nabla \phi + f_w'(\phi) = 0, \tag{10}$$

where $\boldsymbol{v}_w$ is the wall velocity and $\boldsymbol{n}$ is the outward normal vector to the wall (pointing from the fluid into the wall). The second condition represents zero mass flux through the substrate, and the third is a natural boundary condition arising from variation of the wall energy. It implies rapid wall relaxation so that the fluids are at equilibrium with the solid, and the dynamic contact angle remains at the equilibrium value θ_S.[30]

The governing equations together with the boundary conditions are numerically solved with a finite-element package AMPHI, which employs unstructured triangle elements and adaptive meshing. The detailed algorithm was discussed by Yue *et al.*[33] and extensive validations were performed.

The geometry is described by the following length ratios: h/l_g, H/l_g, and $W=l_s/l_g$. In equilibrium, the liquid-gas interface is a circular arc with protrusion angle θ_0. The macroscopic physical parameters can be combined into three dimensionless numbers: the capillary number $\mathrm{Ca}=\mu_l \dot{\gamma}_0 l_g/\sigma$, the viscosity ratio $m=\mu_l/\mu_g$, and the equilibrium contact angle θ_S. The diffuse-interface model introduces two additional dimensionless numbers: the Cahn number $\mathrm{Cn}=\epsilon/l_g$ and $S=\sqrt{M\mu^*}/l_g$ with $\mu^*=\sqrt{\mu_l\mu_g}$. These indicate, respectively, the interfacial thickness and the Cahn–Hilliard *diffusion length* relative to the macroscopic length l_g, with the diffusion length being the counterpart of the "slip length" in sharp-interface models for contact lines.[34,35]

In the computations to be presented, we have fixed $h/l_g=1$, $H/l_g=4$, $\theta_0=45°$, and $\theta_S=120°$. The large static contact angle is motivated by the fact that experiments typically use hydrophobic substrates to ensure the Cassie state. The role of wettability on depinning is easy to anticipate [cf. Eq. (11)] and thus we did not examine other θ_S values. The viscosity ratio between water and air is on the order of 50, and we have used $m=25$ for all the computations except those reported in Fig. 11 for $m=50$. Cn and S values are dictated by the requirements to achieve the *sharp-interface limit* and to accurately capture the effective slip length.[35] We have used $S=0.01$ in all the simulations, and determined the appropriate Cn values through numerical experiments to be discussed shortly. Thus, the main control parameters are Ca and W, and the numerical results are presented largely as a parametric study in the (Ca, W) plane. The initial condition has a linear shear flow in the channel, stationary gas in the grooves, and the equilibrium interfacial shape.

III. RESULTS

A. Sharp interface limit

When using the diffuse-interface model to compute interfacial flows, a key concept is the sharp-interface limit.[35,36] Real interfaces for common fluids have a thickness of nanometers, and usually cannot be resolved in macroscopic flow computations. Thus, one uses unrealistically large values for the capillary width ϵ or the Cahn number Cn. This is permissible if Cn is small enough such that the numerical results no longer depend on it. That is when the sharp-interface limit is attained, where the diffuse-interface theoretical framework is consistent with the classical Navier–Stokes description.

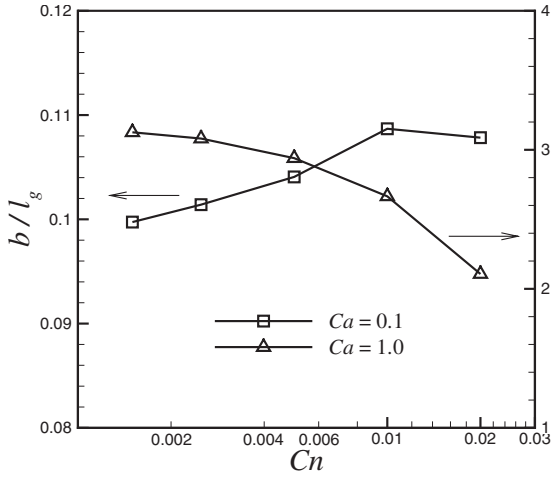

FIG. 2. Variation of the slip length b with the Cahn number Cn at $W=0.5$ and two capillary numbers Ca=0.1 and 1.

For interfacial flows without contact lines, the sharp-interface limit is typically approached at $\mathrm{Cn}\sim 0.01$.[33] Moving contact lines complicate the issue considerably, and the existence of a sharp-interface limit has been established only based on empirical evidence as opposed to analytical proof. For Couette and Poiseuille flows with a transverse interface, Yue *et al.*[35] found that the location of the menisci converges to a unique solution after Cn falls below a threshold $\mathrm{Cn}^c \approx 4S$, and suggested this as the criterion for achieving the sharp-interface limit.

For our problem, this criterion turns out to be too lax. Even though the position of the liquid-gas interface apparently converges for $\mathrm{Cn}<4S=0.04$, the slip length b continues to vary appreciably, as shown in Fig. 2. For the two smallest values tested, Cn=0.0015 and 0.0025, b differs by less than 2% for both Ca=0.1 and 1, the smallest and largest capillary numbers covered in this study. Thus, we have taken Cn=0.0025 to be the threshold for the convergence of the slip length, and used it in all calculations reported hereafter.

The reason that b requires a more stringent Cn criterion than previously suggested has to do with the geometric setup of the problem, and differs somewhat for the two Ca values in Fig. 2. Ca=0.1 corresponds to the so-called regime I (see Sec. III B for details) with a pinned and slightly deformed bubble. In this regime, the slippage is small and very sensitive to minute errors in the interfacial location. One source of error is spontaneous shrinkage due to global energy minimization, which is especially limiting here since the gas bubble is small relative to the surrounding liquid.[37] Thus, smaller Cn is needed for capturing the slip length accurately. The increase in b with increasing Cn in Fig. 2 reflects the fact that more severe bubble shrinkage at higher Cn amounts to decrease in the protrusion angle, which is known to increase the slip length in this regime.[27,38]

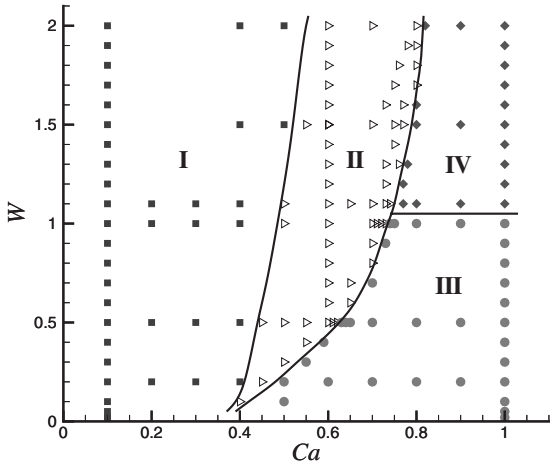

FIG. 3. Phase diagram showing four different flow regimes in the Ca-W plane. The symbols indicate the individual simulations and the solid lines delineate the boundaries between the regimes. Regimes I–III are steady and regime IV is periodic.

The curve for Ca=1 corresponds to regime III, with a thin, continuous gas film covering the solid substrate and producing a much larger slip. The thickness of the gas film δ is far less than the groove width l_g. To compute b accurately, as it turns out, we must require $\epsilon \ll \delta$, a much more stringent condition than $\epsilon \ll l_g$. Otherwise the interfacial diffusion increases the effective viscosity inside the gas film and artificially dampens slippage. This also explains the decrease of b with Cn for Ca=1 in Fig. 2, in contrast to the Ca=0.1 curve.

B. Flow regimes

A detailed parametric investigation of the shear flow over the patterned substrate is performed by varying W and Ca. We observe four flow regimes, depicted by the phase diagram of Fig. 3. Regimes I–III are steady, while regime IV is time periodic.

1. Regime I with pinned contact line

The shear flow exerts a hydrodynamic force on the gas bubble via a pressure normal to the interface and a tangential viscous stress. In the rest of the paper, this hydrodynamic force will be called the "shear force" for brevity. When the shear rate is small, e.g., Ca=0.1, the shear force is much weaker than the capillary force. The bubble is only slightly deformed such that the local protrusion angle θ increases on the downstream side of the bubble and decreases on its upstream side [Fig. 4(a)].

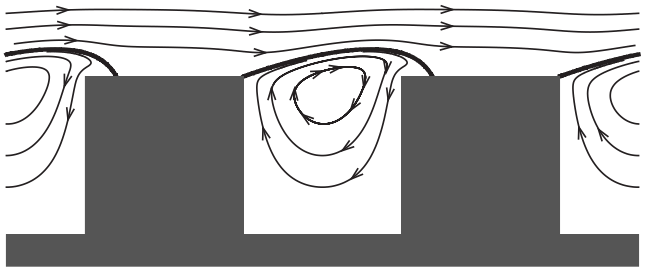

FIG. 5. Steady regime II at $W=1$ and Ca=0.73, with the downstream contact line depinned and shifted downstream.

The pinning of a contact line on sharp corners reflects the degeneracy of the local force balance. It is easy to see in Fig. 4(b) that the contact line is pinned at a 90° protruding corner provided that the protrusion angle θ and contact angle θ_S satisfy the following:[8,39]

$$90^\circ < \theta + \theta_S < 180^\circ, \tag{11}$$

which in our case ($\theta_S=120°$) translates to $-30° < \theta < 60°$. Outside this range, the pinning becomes unstable; if the contact line moves off the sharp corner onto the flat substrate, the local balance among the interfacial forces will favor continued motion in that direction. Thus a contact line can be depinned if the shear force due to the external flow becomes strong enough to drive θ outside the range of Eq. (11). These simple considerations also anticipate the role of substrate wettability. Hydrophobicity lowers the threshold for depinning on the downstream side of the cavity and facilitates the spread of the gas bubble on the substrate.

2. Regime II with depinned contact line

As the shear rate and hence the driving force increase, the bubble deforms more and more until the protrusion angle θ downstream of the bubble exceeds the threshold $180°-\theta_S$ [see Eq. (11)]. The contact line downstream then depins and slides on top of the ridge (Fig. 5). Meanwhile the contact line upstream of the bubble remains pinned because the substrate is poorly wetting for the liquid. This asymmetry can be eas-

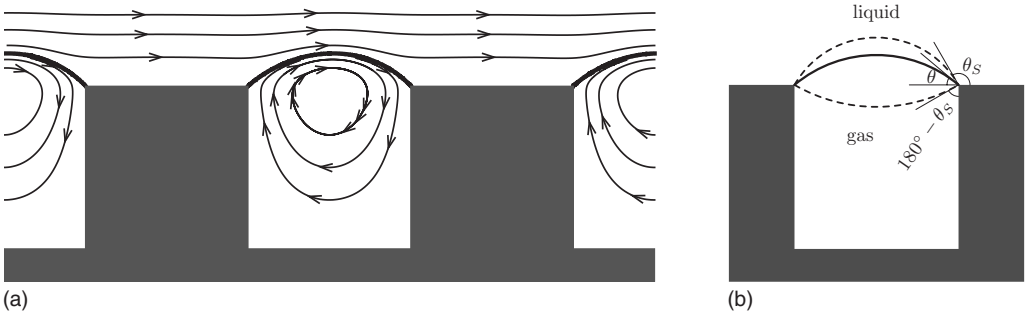

FIG. 4. (a) The steady regime I at $W=1$, Ca=0.1, with the contact line pinned at the edges of the ridge. The menisci are indicated by the thick solid curves while the streamlines by the thin lines. Note the recirculation in the gas. (b) Schematic illustrating the condition for contact line pinning. The dashed curves represent the thresholds of depinning given by Eq. (11).

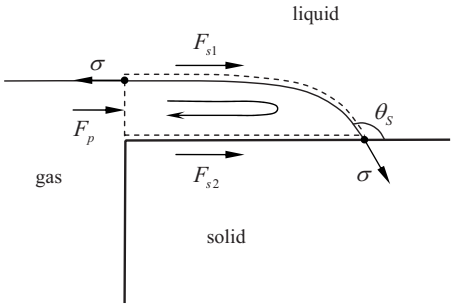

FIG. 6. Schematic illustrating the instability of the meniscus that prompts the transition from regime II to regime III or IV.

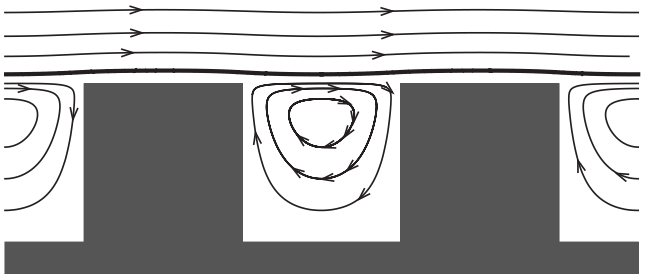

FIG. 7. The steady-state regime III at $W=1$ and Ca=1. The meniscus is flattened by the shear force to form a continuous gas layer.

ily understood from Eq. (11) and Fig. 4(b). As the depinned contact line moves downstream, the bubble effectively spreads on the substrate. This reduces the height of the protruding bubble and the shear force on it. Moreover, the asymmetry in the protruding angle becomes more pronounced, thus increasing the net capillary force that resists further spreading. Therefore, if the shear rate is not too high, a new force balance is attained and the contact line stops at a small distance downstream of the corner. This steady flow is regime II, depicted in Fig. 5 for $W=1$ and Ca=0.73.

Referring to Fig. 3, we note that with $W=1$, the shear rate at Ca=0.73 is very close to the upper bound of regime II. Further increase in Ca will not lead to steady solutions with ever increasing displacement of the contact line downstream. Rather, the steady solution loses stability in a catastrophic change of the interfacial morphology. Two consequences are possible. If the ridge is not too wide ($W \lesssim 1.05$), the contact line rapidly moves downstream and merges with the pinned contact line of the next bubble, forming a continuous gas film covering the top of the ridge. A steady-state solution is then achieved (regime III below). If the ridge is wider ($W \gtrsim 1.05$), the gas film is itself unstable, and periodically breaks up at the upstream corner of the ridge (regime IV).

The destabilization of regime II amounts to a loss of steady position for the downstream contact line, and can be qualitatively understood from the force balance on the meniscus. Consider the control volume enclosed by the dashed line in Fig. 6. We assume that the length of the control volume L is much larger than its thickness d so that the enclosed gas can be regarded as a thin film. For the thin-film meniscus to be steady, the following force balance must be satisfied:

$$F_{s1} + F_{s2} + F_p = \sigma(1 + \cos\,\theta_S), \tag{12}$$

where F_{s1} and F_{s2} are the shear forces exerted by the liquid and the solid, respectively, the latter due to the recirculation within the gas, as shown in Fig. 6. F_p is the force due to the pressure difference. F_{s1} can be estimated from the external shear as $F_{s1} \sim \mu_l \dot{\gamma}_0 L$. Assuming unidirectional flow in the film with zero net mass flux, one easily obtains $F_{s2}=F_{s1}/2$. The capillary pressure has negligible effect since $d \ll L$. Thus the meniscus is governed primarily by the balance between the shear force and the surface tension. However, this balance is unstable. If the contact line is perturbed toward the downstream, the length of the film increases and so do the shear forces. As the surface tension remains the same, the force balance is broken and the contact line would continue to advance. Conversely, a small shift of the contact line upstream would lead to continual receding of the meniscus. The upshot of this analysis is that the contact line cannot have a steady position far downstream of the corner so as to render the meniscus a thin film. It will be either fairly close to the corner, as in regime II (Fig. 5), or rapidly moving downstream to produce regime III or IV.

The force balance of Eq. (12) also informs the intuition that hydrophobicity should assist the spread of the gas film. Together with the contact line depinning criterion discussed above, this suggests that hydrophobicity facilitates the transitions from regime I to II and from regime II to III or IV. As will be shown in Sec. III C, these transitions are accompanied by increased apparent slippage.

3. Regime III with continuous gas film

Regime III features a continuous gas layer on top of the solid ridge as illustrated in Fig. 7. Thus, the liquid is completely insulated by the gas layer from the solid substrate. Typically, the liquid-gas interface bulges slightly on top of the solid ridge but overall stays rather flat. The thickness of the gas film above the ridge δ may be estimated from volume conservation for the gas. The initial volume of the bubble is $l_g^2\chi(\theta_0)+l_g h$, with $\chi(\theta_0)=(2\theta_0-\sin 2\theta_0)/(8\sin^2\theta_0)$. In regime III, the gas volume in the unit cell under a flat interface would be $(l_g+l_s)\delta+l_g h$. Equating the two yields

$$\delta \approx \frac{\chi(\theta_0)}{1+W} l_g. \tag{13}$$

Two points are notable about this equation. First, for typical W and θ_0 values, the thickness of the gas film is much less than l_g. In our diffuse-interface model, therefore, the interfacial thickness must be compared to the local length scale δ, not the global scale l_g or H. This is the reason, as pointed out before, for the much more stringent criterion on Cn for attaining a converged value for the slip length b (see Fig. 2). Second, the amount of available gas (or the static protrusion angle θ_0) determines the thickness δ, which in turn determines the stability of the gas film and the boundary between regimes III and IV in Fig. 3. A larger θ_0, for instance, stabilizes the gas film and favors regime III.

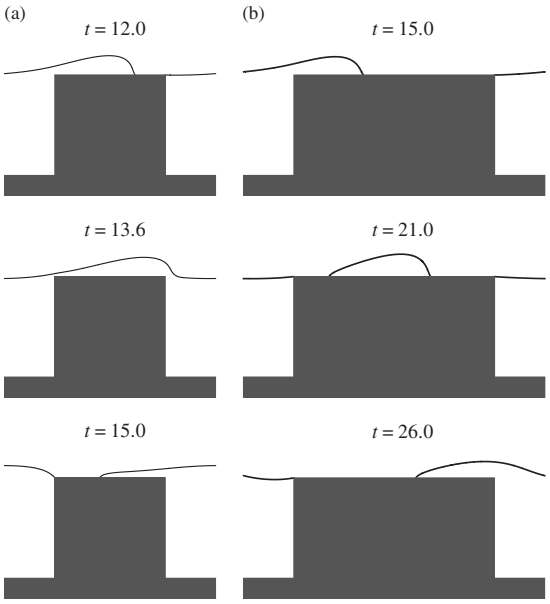

FIG. 8. Snapshots of the periodic regime IV for Ca=1 and (a) $W=1.1$; (b) $W=2$. Time has been made dimensionless by $\dot{\gamma}_0$.

4. Regime IV with periodic bubble detachment

The steady flow regimes discussed above cannot be observed when both Ca and W are large, as shown in Fig. 3. Instead, the flow evolves to a periodic regime IV in this parametric region. Depending on the ridge width W, regime IV can be manifested by one of two periodic scenarios (Fig. 8). For relatively narrow ridges (e.g., $W=1.1$), a continuous gas layer forms temporarily after the advancing contact line coalesces with the downstream bubble [$t=13.6$ of Fig. 8(a)]. However, the gas layer is unstable and breaks up at the upstream edge of the ridge. After that, the gas meniscus on top of the ridge moves rapidly downstream, driven by capillary and shear forces, and merges into the downstream groove. This process then starts anew and produces a time-periodic behavior.

For $W=2$, the ridge is so wide that a continuous gas film cannot be formed. The "finger" of gas on top of the ridge detaches from the upstream groove before its advancing front merges into the downstream groove [$t=21.0$ of Fig. 8(b)]. Thus an isolated gas bubble is produced and it slides on top of the ridge owing to the shear force. Eventually, the bubble coalesces with the gas pocket in the downstream groove and the process repeats itself. Evidently, the boundary between the two periodic scenarios depends on the initial amount of gas or the static protrusion angle θ_0; other conditions being equal, larger θ_0 is conducive to the first while smaller θ_0 to the second.

To some degree, the initial condition affects which flow regime is realized at a certain Ca. Our discussion of flow regimes follows an increasing Ca. If one starts with a gas film as in regime III and gradually reduces Ca, the film will remain linearly stable, in the absence of gravity, even as the external flow vanishes. Such a scenario can be considered a kind of hysteresis but is not very interesting in our context.

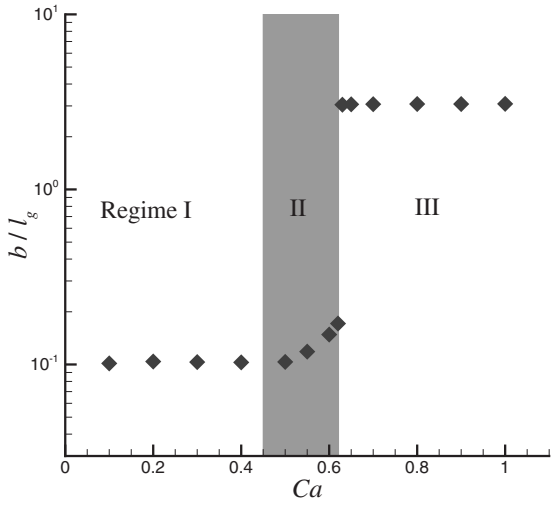

FIG. 9. The slip length b as a function of Ca at $W=0.5$.

The transitions between regimes I and II, and between II and IV, are governed by a clear-cut force balance at the contact line, and no hysteresis is expected.

C. Slip length

As stated at the beginning, the slip being considered here is an "apparent" slip due to the presence of low-viscosity gas that cushions the liquid from the solid substrate. Thus, the amount of slippage should be determined to a large extent by the shape and position of the gas-liquid interface, which in turn depends on the capillary number and the geometric pattern on the substrate, among other things. In the following, we will examine the slip length b in the four flow regimes parametrized by the capillary number Ca and the ridge-groove length ratio W.

1. Effect of Ca

Figure 9 plots the slip length b as a function of the capillary number Ca for a relatively narrow ridge with $W=0.5$. With increasing Ca, the system traverses the three steady flow regimes in turn. In regime I (roughly $\mathrm{Ca} \leq 0.4$), the slip length is small and essentially constant, indicating an independence on the shear rate when the shear rate is relatively low. In this regime, the only effect of the flow is to deform the interface slightly. In regime II, there is a marked increase in b with increasing shear rate. This reflects the gradual advance of the depinned contact line downstream. Thus, the fraction of the substrate exposed to the liquid decreases with Ca, and more liquid can slide on top of the gas.

The small slip length in regime I is in agreement with prior numerical results at low Ca.[27,38] However, the rise of b for larger Ca forms an interesting contrast with the finding of Hyväluoma and Harting.[27] This is because in their setup the contact line is always pinned by the edge of the cavity, and at larger Ca the meniscus is deformed severely by the shear force, with a prominent hump on its downstream side jutting into the liquid. This amounts to additional roughness resisting the liquid flow. Thus, their slip length decreases with the shear rate and even becomes negative for large Ca (see their

Fig. 3). In our computations, the shear force on the meniscus is alleviated by depinning and displacement of the downstream contact line before the interface deforms greatly.

The discontinuous transition from regime II to III is accompanied by a *discontinuous jump* in b by a factor of 18 (Fig. 9). Within regime III, the slip length is once again independent of the shear rate, similar to regime I. The jump is evidently due to the formation of the gas film that completely covers the top of the ridge, thus preventing any liquid-solid contact. The magnitude of the jump and the constant b in regime III depends on W and the viscosity ratio m, and a scaling relationship will be derived in Sec. III C 2. The significant slip of regime III is reminiscent of water-lubricated pipelines for transporting crude oil,[40] both bringing about remarkable reduction in wall friction. For example, a slip length $b=3l_g$ corresponds to a 43% drag reduction for the flow geometry considered. Such enhanced slippage may be beneficial to delivering liquids through narrow microfluidic channels.

When W is sufficiently large, the periodic regime IV prevails at higher Ca, and imparts different features to b, as illustrated in Fig. 10. Similar to Fig. 9, the slip length is mostly constant in regime I, increases with the shear rate in regime II, and experiences a steep increase at the transition from regime II to regime IV. In regime IV, b varies periodically [Fig. 10(b)], with sharp peaks coinciding with intervals when the solid substrate is completely enveloped in gas [cf. Fig. 8(a)]. Thus, the data points in Fig. 10(a) are based on averaging over a period T. First, note that in comparison with regime III (Fig. 9), b in regime IV is much smaller. This is evidently because the liquid is not completely insulated from the solid substrate for much of each period. Second, b exhibits a significant increase with Ca in regime IV, in contrast to regime III. At lower shear rate or Ca, the meniscus moves more slowly and the period T is longer [Fig. 10(b)]. Thus, the spikes of b, corresponding to the temporary full coverage of the solid by the gas, take up a smaller fraction of T, with the result of a smaller mean slip length. Finally, the period T tends to infinity as Ca approaches the lower bound of regime IV. The b spikes become so infrequent that their contribution to the averaged slip length tends to nil. This argument suggests that b should vary continuously at the transition between regimes II and IV, again in contrast to the II-III transition. At larger W values, the periodic scenario of Fig. 8(b) prevails, with slightly different time-periodic behaviors of b. This will be discussed in Sec. III C 2.

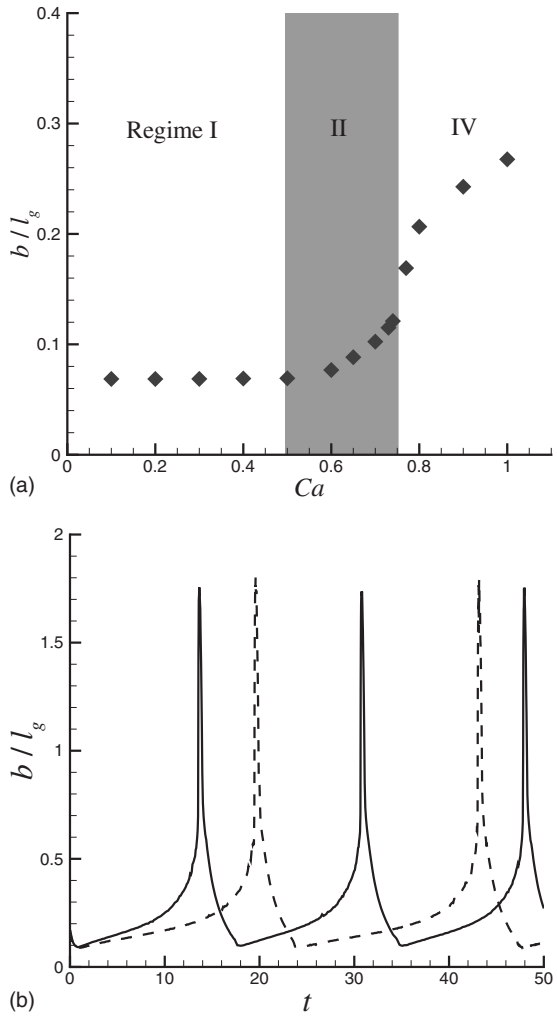

FIG. 10. (a) The slip length b as a function of Ca at $W=1.1$. In regime IV, b is averaged over one period. (b) Time history of b in regime IV for Ca $=0.9$ (dashed line), 1 (solid line) and $W=1.1$. Time is made dimensionless by $\dot{\gamma}_0$.

2. Effect of W

To investigate the effect of substrate pattern on slip, we varied W in each flow regime with a fixed Ca. In Fig. 11(a), regimes I and II are realized at two Ca values, Ca=0.1 and 0.6. In Fig. 11(b), on the other hand, regime III transitions into IV with increasing W at the same Ca=1. Note that in regime IV, b is the mean slip length averaged over a period. In all cases, b decreases monotonically with W. For regime I, the decrease is easily understood since a larger W corresponds to a larger solid-area fraction of the substrate. For regime II, the same reason holds. Moreover, a larger W reduces the liquid velocity near the substrate. This hampers the downstream displacement of the contact line and further enlarges the solid exposure to the liquid. For regime III, b is closely related to the thickness of the gas film δ [Eq. (13)] on top of the solid ridge, a thinner film at larger W corresponding to a smaller slip length.

Regime IV deserves special attention because of the periodic nature of the interfacial evolution. Note first that the transition from regime III to IV, at $W\approx 1.05$ in Fig. 11(b), results in a large and *discontinuous* drop in b. This is evidently owing to the loss of a continuous gas film that covers the solid in all times. Within regime IV, b continues to decline gradually with W. This can be understood from the temporal variation of b in Fig. 12. For the relatively narrow $W=1.1$, b has a single peak in each period due to the transient appearance of a continuous gas film [cf. Figs. 8(a) and 10(b)]. For $W=1.4$ and 2, however, two much lower peaks appear in each period, corresponding to the detachment of the gas bubble from the upstream groove and its subsequent merging into the downstream groove [Fig. 8(b)]. As the ridge widens, not only does the period lengthen but the peaks of

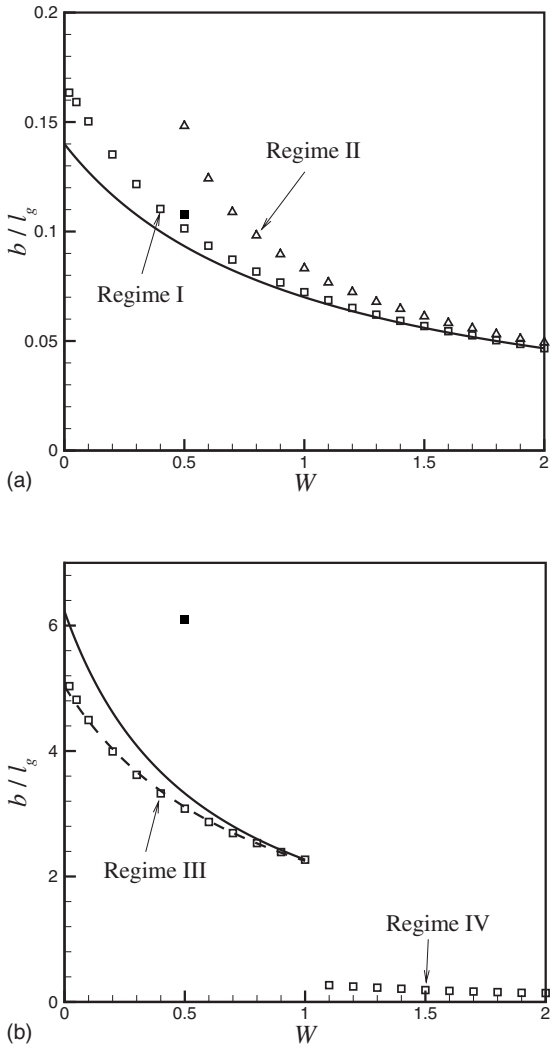

FIG. 11. The slip length b as functions of W. (a) Ca=0.1 (squares, regime I) and Ca=0.6 (triangles, regime II). The solid curve depicts Eq. (14) with $\alpha=0.14$ for regime I. (b) Ca=1 (squares, regimes III and IV). The solid curve represents Eq. (15) with $\beta=0.57$, while the dashed curve Eq. (16) for $\beta=0.71$ and $\xi=0.88$. The filled squares give b at an elevated viscosity ratio $m=50$, $W=0.5$ and (a) Ca=0.1, (b) Ca=1.

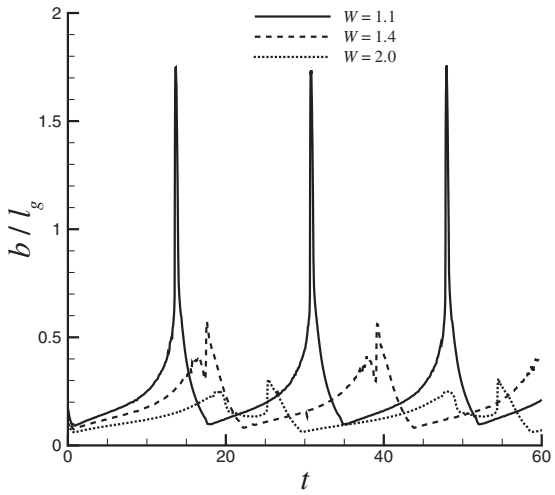

FIG. 12. Time history of the slip length b in regime IV for Ca=1 and typical values of W.

the slip length also become lower. Both factors contribute to the decline of the averaged b with W.

A more quantitative understanding can be gained via $b \sim W$ scaling relationships. If the liquid-gas interface is flat ($\theta_0=0°$) and bears zero shear stress, the slip length can be calculated analytically.[21,41,42] However, due to the meniscus curvature and the gas dissipation, no analytical solution is available in our case. For regime I, we borrow a scaling relationship that Ybert *et al.*[22] developed for the limit of large W and zero protrusion angle,

$$b = \frac{\alpha}{1+W} l_g, \tag{14}$$

where α is a fitting parameter. This is based on averaging the finite slip over the groove and the zero slip over the solid ridge. When applied to our geometry, the parameter α accounts for the protruding meniscus. Figure 11(a) shows that $\alpha=0.14$ provides a reasonable representation of the numerical results; the agreement is excellent for wider ridges with $W>1$.

Similarly, a scaling relationship can be derived to describe the decrease in b with W in regime III. As Fig. 7 shows, the liquid-gas interface is mostly flat in this regime and moves with a velocity V that is essentially constant. Thus, the slip length b can be estimated from the effective shear stress on the horizontal plane flush with the top of the ridge. For the part over the solid ridge, the shear stress in the thin gas film may be approximated as $\tau_s=\mu_g V/\delta$, provided that W is not too small. For the part over the groove, the shear stress is reduced because of the circulating vortex underneath, and can be written as $\tau_g=\beta\tau_s$, with $\beta<1$ being an *ad hoc* constant. Now the mean shear stress on the horizontal plane flush with the ridge can be obtained as $\tau_e=(\tau_s l_s+\tau_g l_g)/(l_s+l_g)=(\mu_g V/\delta)(W+\beta)/(W+1)$. Since the mean shear stress can also be written as $\mu_l V/b$, we arrive at the following equation for the slip length b:

$$b = \frac{m\chi(\theta_0)}{W+\beta} l_g, \tag{15}$$

where Eq. (13) has been used for δ. The constant β can be determined by equating the model prediction to the computed b at the maximum $W=1$ for regime III: $\beta=0.57$. With this the scaling law is plotted in Fig. 11(b) as the solid curve, which adequately represents the trend of the numerical data. The quantitative overprediction of b amounts to underestimating the mean shear stress. This may be due to the omission of the "end effects" for the gas film and waviness of the gas-liquid interface, both being more pronounced for narrower ridge with relatively small W. Accounting for such corrections by a second fitting parameter ξ, a modified scaling relationship

$$b = \frac{m\chi(\theta_0)}{\xi W+\beta} l_g \tag{16}$$

fits the data very well in regime III, even for small W values. In this case the best fitting parameters are $\beta=0.71$ and $\xi=0.88$.

The scaling for regimes I and III differs markedly in the role of the viscosity ratio m. In Eq. (15), for regime III, b is proportional to m, while in Eq. (14), for regime I, b does not explicitly depend on m. So far, the reported simulations all have $m=25$. To check the m dependence, we have doubled the viscosity ratio to $m=50$ and solved the problem for $W=0.5$. The computed slip length is denoted by the solid squares in Fig. 11. In regime I, the slip length is very close to that of $m=25$ and thus insensitive to the viscosity ratio. In contrast, the slip length is approximately doubled in regime III in accordance with Eq. (15).

D. Concluding remarks

We have performed numerical simulations of the effective slippage of a viscous liquid over a textured substrate with entrapped microbubbles protruding into the liquid. The diffuse-interface model not only captures the liquid-gas interface accurately but also handles the moving contact line efficiently. The most important finding is that depinning and subsequent movement of the contact line on the solid can greatly enhance the apparent slippage on patterned substrates. More specifically, the results can be summarized as follows.

(a) Depending on the capillary number Ca and the solid-to-cavity length ratio W, three steady and one time-periodic flow regimes may appear. At low shear rates, the deformation of the menisci is small and the contact lines remain pinned at the corners of the cavity (regime I). Higher shear rates can depin the contact line downstream of the gas bubble and move it progressively downstream (regime II). At even higher shear rates, the depinned contact line merges into the downstream bubble, producing a continuous gas film cushioning the liquid from the substrate (regime III). If both Ca and W are large, the gas film loses stability and undergoes cycles of breakup and recoalescence, leading to a time-periodic flow (regime IV).

(b) The apparent slip length b is shear independent in regime I but increases with Ca in regime II after the contact line depins. The transition to regime III or IV is accompanied by a giant increase in b. In the steady regime III, b is again shear independent. In the periodic regime IV, b continues to increase with Ca. Scaling relations may be derived for some of the regimes that capture the dependence of b on the liquid-gas viscosity ratio and the geometric parameter W.

Note that these results depend on sufficient amount of gas being trapped in isolated cavities. In an experiment, less gas may be trapped initially or the gas may escape into the liquid by diffusion.[29] If the meniscus does not protrude into the liquid, transition to the gas film cannot occur and neither can the enhanced apparent slippage. Moreover, substrate textures made of posts or pillars allow the trapped gas to be interconnected, and the mechanism for slippage and superhydrophobicity will be different on such substrates.

As stated at the outset, this work was motivated chiefly by the disagreement among previous work on the shear dependence of the apparent slip. The trend predicted—b being shear-independent at low Ca and increasing with Ca at higher Ca—is consistent with experimental evidence. For example, experiments in microfluidic channels typically produce a constant b for shear rates $\dot{\gamma}<10^2$ s^{-1},[13,24] but an increasing b for $\dot{\gamma}\sim10^5$ s^{-1}.[4] The increase in b with Ca also agrees qualitatively with the AFM experiments of Zhu and Granick.[6,28]

A more quantitative comparison with experiments is hampered by a mismatch of parameters. Given the small dimensions in microfluidic devices, exceedingly high shear rates are needed to produce Ca high enough to deform the menisci. For instance, taking our bubble length scale to be $l_g=1$ μm for a water-air system with liquid viscosity $\mu_l=10^{-3}$ Pa s and surface tension $\sigma=72$ dyn/cm, our shear rate $\dot{\gamma}$ should range from 10^6 to 10^7 s^{-1} for $0.1<\mathrm{Ca}<1$. In most experiments, the achievable shear rates are much lower. Therefore, our computations probably explain why the shear dependence of the slip length has *not* been detected in most experiments. As for the observed b(Ca) dependence at larger Ca,[4,28] the role of contact line depinning and motion remains to be ascertained.

New experiments can be designed to probe the parameter range relevant to contact line depinning and motion. Coarser textures and greater gas fraction will be beneficial.[14] The requirement on shear rate can also be relaxed by using liquids of higher viscosity. For example, taking glycerol ($\mu_l=1.5$ Pa s and $\sigma=64$ dyn/cm) as the test liquid, the corresponding shear rates can be reduced to 10^3–10^4 s^{-1}, which is comparable with those achieved in the experiments of Steinberger *et al.*[26] and Choi *et al.*,[4] although they used less viscous liquids. We hope that the present work will motivate new experiments to investigate the mechanism of contact line depinning and further clarify the dependence of apparent slip on shear rates.

ACKNOWLEDGMENTS

We acknowledge support by the Petroleum Research Fund, the Canada Research Chair program, NSERC (Discovery and Strategic grants), CFI, and NSFC (Grant Nos. 50390095 and 20674051). We thank Professor Neelesh Patankar (Northwestern University) and Professor Pengtao Yue (Virginia Tech.) for discussions.

[1] C. Neto, D. R. Evans, E. Bonaccurso, H. J. Butt, and V. S. J. Craig, "Boundary slip in Newtonian liquids: A review of experimental studies," Rep. Prog. Phys. **68**, 2859 (2005).
[2] E. Lauga, M. P. Brenner, and H. A. Stone, "Microfluidics: The no-slip boundary condition," in *Handbook of Experimental Fluid Dynamics* (Springer, New York, 2005), Chap. 15.
[3] V. S. J. Craig, C. Neto, and D. R. M. Williams, "Shear-dependent boundary slip in an aqueous Newtonian liquid," Phys. Rev. Lett. **87**, 054504 (2001).
[4] C. H. Choi, K. J. A. Westin, and K. S. Breuer, "Apparent slip flows in hydrophilic and hydrophobic microchannels," Phys. Fluids **15**, 2897 (2003).
[5] C. Cottin-Bizonne, A. Steinberger, B. Cross, O. Raccurt, and E. Charlaix, "Nanohydrodynamics: The intrinsic flow boundary condition on smooth surfaces," Langmuir **24**, 1165 (2008).
[6] Y. X. Zhu and S. Granick, "Rate-dependent slip of Newtonian liquid at smooth surfaces," Phys. Rev. Lett. **87**, 096105 (2001).

[7]D. C. Tretheway and C. D. Meinhart, "Apparent fluid slip at hydrophobic microchannel walls," Phys. Fluids **14**, L9 (2002).
[8]D. Quere, "Wetting and roughness," Annu. Rev. Mater. Res. **38**, 71 (2008).
[9]P. G. de Gennes, "On fluid/wall slippage," Langmuir **18**, 3413 (2002).
[10]D. C. Tretheway and C. D. Meinhart, "A generating mechanism for apparent fluid slip in hydrophobic microchannels," Phys. Fluids **16**, 1509 (2004).
[11]J. W. G. Tyrrell and P. Attard, "Atomic force microscope images of nanobubbles on a hydrophobic surface and corresponding force-separation data," Langmuir **18**, 160 (2002).
[12]P. A. Thompson and S. M. Troian, "A general boundary condition for liquid flow at solid surfaces," Nature (London) **389**, 360 (1997).
[13]J. Ou, B. Perot, and J. P. Rothstein, "Laminar drag reduction in microchannels using ultrahydrophobic surfaces," Phys. Fluids **16**, 4635 (2004).
[14]C. Lee, C. H. Choi, and C. J. Kim, "Structured surfaces for a giant liquid slip," Phys. Rev. Lett. **101**, 064501 (2008).
[15]P. Joseph, C. Cottin-Bizonne, J. M. Benoit, C. Ybert, C. Journet, P. Tabeling, and L. Bocquet, "Slippage of water past superhydrophobic carbon nanotube forests in microchannels," Phys. Rev. Lett. **97**, 156104 (2006).
[16]C. H. Choi, U. Ulmanella, J. Kim, C. M. Ho, and C. J. Kim, "Effective slip and friction reduction in nanograted superhydrophobic microchannels," Phys. Fluids **18**, 087105 (2006).
[17]D. Byun, J. Kim, H. S. Ko, and H. C. Park, "Direct measurement of slip flows in superhydrophobic microchannels with transverse grooves," Phys. Fluids **20**, 113601 (2008).
[18]C. Cottin-Bizonne, J. L. Barrat, L. Bocquet, and E. Charlaix, "Low-friction flows of liquid at nanopatterned interfaces," Nat. Mater. **2**, 237 (2003).
[19]J. Davies, D. Maynes, B. W. Webb, and B. Woolford, "Laminar flow in a microchannel with superhydrophobic walls exhibiting transverse ribs," Phys. Fluids **18**, 087110 (2006).
[20]D. Maynes, K. Jeffs, B. Woolford, and B. W. Webb, "Laminar flow in a microchannel with hydrophobic surface patterned microribs oriented parallel to the flow direction," Phys. Fluids **19**, 093603 (2007).
[21]E. Lauga and H. A. Stone, "Effective slip in pressure-driven Stokes flow," J. Fluid Mech. **489**, 55 (2003).
[22]C. Ybert, C. Barentin, C. Cottin-Bizonne, P. Joseph, and L. Bocquet, "Achieving large slip with superhydrophobic surfaces: Scaling laws for generic geometries," Phys. Fluids **19**, 123601 (2007).
[23]C. H. Choi and C. J. Kim, "Large slip of aqueous liquid flow over a nanoengineered superhydrophobic surface," Phys. Rev. Lett. **96**, 066001 (2006).
[24]R. Truesdell, A. Mammoli, P. Vorobieff, F. van Swol, and C. J. Brinker, "Drag reduction on a patterned superhydrophobic surface," Phys. Rev. Lett. **97**, 044504 (2006).
[25]E. Lauga and M. P. Brenner, "Dynamic mechanisms for apparent slip on hydrophobic surfaces," Phys. Rev. E **70**, 026311 (2004).
[26]A. Steinberger, C. Cottin-Bizonne, P. Kleimann, and E. Charlaix, "Nanoscale flow on a bubble mattress: Effect of surface elasticity," Phys. Rev. Lett. **100**, 134501 (2008).
[27]J. Hyväluoma and J. Harting, "Slip flow over structured surfaces with entrapped microbubbles," Phys. Rev. Lett. **100**, 246001 (2008).
[28]Y. X. Zhu and S. Granick, "Limits of the hydrodynamic no-slip boundary condition," Phys. Rev. Lett. **88**, 106102 (2002).
[29]N. A. Patankar, "Hydrophobicity of surfaces with cavities: Making hydrophobic substrates from hydrophilic materials," J. Adhes. Sci. Technol. **23**, 413 (2009).
[30]D. Jacqmin, "Contact-line dynamics of a diffuse fluid interface," J. Fluid Mech. **402**, 57 (2000).
[31]T. Z. Qian, X. P. Wang, and P. Sheng, "A variational approach to moving contact line hydrodynamics," J. Fluid Mech. **564**, 333 (2006).
[32]C. F. Zhou, P. T. Yue, and J. J. Feng, "3D phase-field simulations of interfacial dynamics in Newtonian and viscoelastic fluids," J. Comput. Phys. (to be published).
[33]P. T. Yue, C. F. Zhou, J. J. Feng, C. F. Ollivier-Gooch, and H. H. Hu, "Phase-field simulations of interfacial dynamics in viscoelastic fluids using finite elements with adaptive meshing," J. Comput. Phys. **219**, 47 (2006).
[34]R. G. Cox, "The dynamics of the spreading of liquids on a solid surface. Part 1. Viscous flow," J. Fluid Mech. **168**, 169 (1986).
[35]P. Yue, C. Zhou, and J. J. Feng, "Sharp interface limit of the Cahn–Hilliard model for moving contact lines," J. Fluid Mech. (to be published).
[36]G. Caginalp and X. F. Chen, "Convergence of the phase field model to its sharp interface limits," Eur. J. Appl. Math. **9**, 417 (1998).
[37]P. T. Yue, C. F. Zhou, and J. J. Feng, "Spontaneous shrinkage of drops and mass conservation in phase-field simulations," J. Comput. Phys. **223**, 1 (2007).
[38]A. Steinberger, C. Cottin-Bizonne, P. Kleimann, and E. Charlaix, "High friction on a bubble mattress," Nature Mater. **6**, 665 (2007).
[39]J. F. Oliver, C. Huh, and S. G. Mason, "Resistance to spreading of liquids by sharp edges," J. Colloid Interface Sci. **59**, 568 (1977).
[40]D. D. Joseph, "Lubricated pipelining," Powder Technol. **94**, 211 (1997).
[41]J. R. Philip, "Flows satisfying mixed no-slip and no-shear conditions," Z. Angew. Math. Phys. **23**, 353 (1972).
[42]J. R. Philip, "Integral properties of flows satisfying mixed no-slip and no-shear conditions," Z. Angew. Math. Phys. **23**, 960 (1972).